I&EC research
Industrial & Engineering Chemistry Research

pubs.acs.org/IECR
Article

Liquid Fluidization of Short Hollow Cylinders

Jacobus Johannes Derksen*

Cite This: *Ind. Eng. Chem. Res.* 2023, 62, 19197−19204
Read Online

ABSTRACT: We perform numerical simulations on fluidized dense suspensions of solid spheres, solid cylinders, and hollow cylinders in a Newtonian liquid. The simulations are three-dimensional and time-dependent and aim to resolve the flow around and—for the hollow particles—inside individual particles. We use a lattice-Boltzmann scheme that includes an immersed boundary approach for imposing no-slip at solid surfaces. The overall solids volume fraction is 0.5 for the solid particles and 0.375 for hollow cylinders. The latter have a length over outer diameter aspect ratio in the range of 0.56−1.58, while the ratio of outer to inner diameter is 2. Archimedes numbers of the order 10^3−10^4 are such that we expect inhomogeneous fluidization with wave-type voidage instabilities. We have a particular interest in the flow through the inner diameter of the hollow cylinders and the extent to which it could contribute to liquid−solid mass transfer.

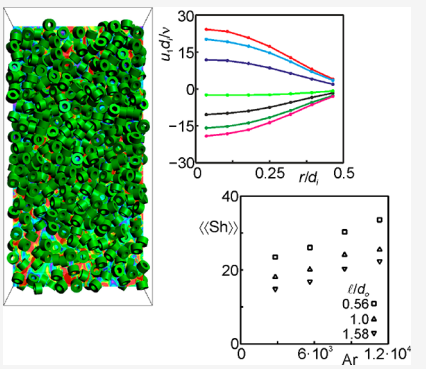

1. INTRODUCTION

Fixed and fluidized beds are workhorses for achieving mass and heat transfer in many industrial applications and therefore are the subject of an extensive body of research, design, and technological development. A primary application of gas fluidization is fluid catalytic cracking.[1] A trickle bed reactor is an example of a fixed bed with the solids providing surface area for heterogeneous reactions of species contained in a gas and in a liquid phase.[2] Liquid fluidization is used for purposes such as particle classification and backwashing of filter material.[3] It also is an important test bed for fundamental studies on the onset and characterization of instabilities in fluidization.[4,5]

In fixed beds, the design of particle shapes with the aim of enhancing their transfer performance is an active area of research of an experimental[6] as well as computational nature.[7] In fluidization, the motivation for studying particles with shapes (very) different from spheres usually is the feedstock supplied to the process. A prominent example is biomass conversion[8] with the biomass in the form of a fibrous particulate material. To enable fluidization of biomass, it often is co-fluidized with sand particles.[9,10]

The author is not aware of studies on the design of shapes of particles (other than spherical) to be used in fluidization and with the aim of enhancing transfer properties or flow characteristics. One likely reason for this is concern about the mechanical strength of the particles.[11] Given frequent and potentially vigorous collisions between particles in dense fluidized beds, breakage and attrition of particles might render the benefits of a carefully designed particle shape ineffective. Despite such concern it seems a useful exercise to probe potential benefits of particle shape in fluidization, specifically when it comes to mass transfer performance.

The above is the motivation of this paper. It describes a purely computational exercise on, eventually, the contribution of the flow within the internal diameter of a hollow cylindrical particle to mass transfer in a liquid fluidized bed. One reason to consider liquid fluidization is to ground the fluidization characteristics in experimental data from the literature[4] and to build upon previous computational work of ours.[12] The hollow cylinders are short (length over outer diameter aspect ratio up to ∼1.6) and relatively thick-walled (outer over inner diameter equal to 2) in order to try not to compromise their potential for mechanical strength.

We first study fluidization of a liquid−solid system with spherical particles all having the same size and demonstrate that the simulations quantitatively correctly exhibit the wave instability observed in experiments.[4] In the second step we replace the spheres by solid cylinders with aspect ratio 1 and volume equal to the spheres and generate a similar instability which is—admittedly only circumstantial—evidence that we are able to deal realistically with nonspherical particle fluidization in our simulation methodology. The third step is to fluidize hollow cylinders that, again, show wave instabilities under certain circumstances. With the hollow cylinders we embark on a parameter study in which we vary the length over diameter ratio of the cylinders as well as the Archimedes number and focus on the flow inside their inner diameter and its potential

Special Issue: Vivek Ranade Festschrift

Received: December 10, 2022
Revised: January 18, 2023
Accepted: January 19, 2023
Published: January 31, 2023

https://doi.org/10.1021/acs.iecr.2c04464
Ind. Eng. Chem. Res. 2023, 62, 19197−19204

consequences for solid−liquid mass transfer at the inner cylinder surface.

Since particle shape is the primary focus of this paper, our simulations must be able to resolve the fluid flow around the individual particles. This thus requires what has been termed PRS (particle-resolved simulation);[13] the grid on which fluid flow is solved has a spacing that is smaller by 1 order of magnitude as compared to the particle length-scales so that no-slip at particle surfaces can be imposed explicitly. PRS with spherical and nonspherical particles is a quickly growing branch in multiphase flow research. Given their relevance in process engineering, the motivation of many PRS's comes from gas−solid systems, with studies that include (reactive) gas−solid heat and mass transfer.[14−18] Simulations of gas flow through static assemblies of particles are not only relevant for fixed bed reactors. Given the high Stokes numbers associated with particles suspended in gases, the time scales on which particle assemblies evolve are much larger than flow time scales, which renders credit to a static particle approach in the first instance. This is different for solid−liquid systems that have Stokes numbers of order unity which create a tighter coupling between fluid and solids dynamics and the need for simulations in which the suspended particles freely translate, rotate, and collide. Compared to solid−gas systems, inclusion of mass transfer is more challenging for solid−liquid systems. With Schmidt numbers (Sc) of order 1, as for gases, the resolution requirements for numerically solving scalar transport are comparable to those for fluid dynamics. Liquids have Sc ≫ 1 and therefore need significantly higher resolution, at least for the scalar transport part of the simulation approach.[19]

PRS's are computationally expensive on a per-particle basis (of the order of 10^3−10^4 grid cells/nodes per particle for resolving their interaction with fluid flow), which means that we cannot even simulate a lab-scale fluid bed. Instead we perform simulations in triperiodic domains containing ∼3000 particles that mimic a sample away from walls and internals in a larger fluidized system.

2. FLOW SYSTEM

The flow domain is periodic in all three Cartesian coordinate directions. Its size is $nx \times ny \times nz$ with $nx = ny = nz/2$ and gravity acting in the negative z-direction ($\mathbf{g} = -g\mathbf{e}_z$). It contains Newtonian fluid with kinematic viscosity ν and density ρ as well as n identical solid particles. Three types of particles have been considered: solid spheres with diameter d; solid cylinders with diameter d_c and length l; and hollow cylinders with outer diameter d_o, inner diameter d_i, and length l. The density of the particles is denoted as ρ_s. We define the density ratio as $\gamma = \rho_s/\rho$. In all cases $\gamma > 1$. Given the different types of particles, the Archimedes number is defined based on particle volume V: $\mathrm{Ar} = (\gamma - 1)gV/\nu^2$. This makes for fairer comparison between particles of different shape in systems having the same Ar. The overall solids volume fraction is $\langle\phi\rangle = nV/(nx \cdot ny \cdot nz)$. To maintain an overall force balance over the periodic system, the net gravity felt by the particles is compensated for by a body force on the fluid acting in the positive z-direction: $\mathbf{f} = \langle\phi\rangle(\gamma - 1)\rho g\mathbf{e}_z$.[12]

3. SIMULATION PROCEDURE

The systems considered are inherently three-dimensional and time-dependent, and so are the simulations. The simulations are particle-resolved with particles free to move and rotate; the dimensions of the particles are significantly larger than the spacing of the mesh on which the fluid flow is solved. We then are able to explicitly impose no-slip at the surfaces of the particles and thus account for the actual shape of the particles moving through the fluid.

The five key elements of the simulation procedure are (1) the flow solver that includes (2) an immersed boundary method[20] for imposing no-slip at particle surfaces; (3) solvers for the particle translational and rotational dynamics including (4) close-range interaction forces and collision forces between particles; (5) the kinematics of particle motion which is straightforward for translation but less so for keeping track of particle orientation for which quaternions[21] have been used. This procedure has been followed in a number of our recent papers. The details, including parameter settings, are available in ref 22. The Supporting Information gives further details about the close-range interaction and collision forces. Below is a brief overview guided by the five elements identified above.

(1) The flow solver is based on the lattice-Boltzmann scheme as proposed in refs 23 and 24. An important feature is that it operates on a uniform cubic lattice with spacing Δ, with distribution functions defined in nodes at the (cubic) cell centers. Flow variables such as velocity, pressure, and viscous stress are derived from the distribution functions.[25] The flow evolves in time explicitly with a time step Δt according to a discrete form of the Boltzmann equation.[25]

(2) An immersed boundary method imposes no-slip at the solid particle surfaces. For this the surfaces are represented by a set of off-lattice marker points with nearest neighbor spacing in the range of 0.5−0.6Δ. The fluid velocity at the marker points is determined through interpolation from the lattice nodes and compared to the solid surface velocity. A force on the fluid is applied at each marker point that drives the difference between fluid and solid surface velocity to zero at that surface location.[26] Integration of the force distribution over each particle surface results in the force and torque exerted by the fluid on each particle.

(3) Newton's (translation) and Euler's (rotation) equations are solved by explicit, split-derivative time stepping[27] so as to update linear and angular velocities of the particles. The time step is the same as the time step Δt that updates the flow field. The forces contained in Newton's equation are the hydrodynamic force provided by the immersed boundary method, net gravity, and close-range interaction forces, to be discussed directly below. The torques in Euler's equation are the hydrodynamic torque from the immersed boundary method and the torque stemming from close-range interaction. To make use of the symmetry properties of the particles, the equations of rotational motion are solved in a reference frame attached to the each particle.

(4) Close-range interaction and contact forces have two functions. In the first place, they compensate for a lack of grid resolution. When the surfaces of two different particles moving relative to one another come within a distance Δ, the flow solver is not able anymore to accurately capture the fluid flow in the space between them and therefore their hydrodynamic interaction. To compensate for this, a lubrication force is added to the equations of motion for each of the two particles.[28] In the second place, they perform a "dry" collision between particles and thereby prevent overlap of their volumes. For this, a repulsive elastic spring force is activated upon the distance between two particles falling below 0.15Δ (which is of the order of 10^{-2} times the particle size). Collision detection for cylinders

https://doi.org/10.1021/acs.iecr.2c04464
Ind. Eng. Chem. Res. 2023, 62, 19197−19204

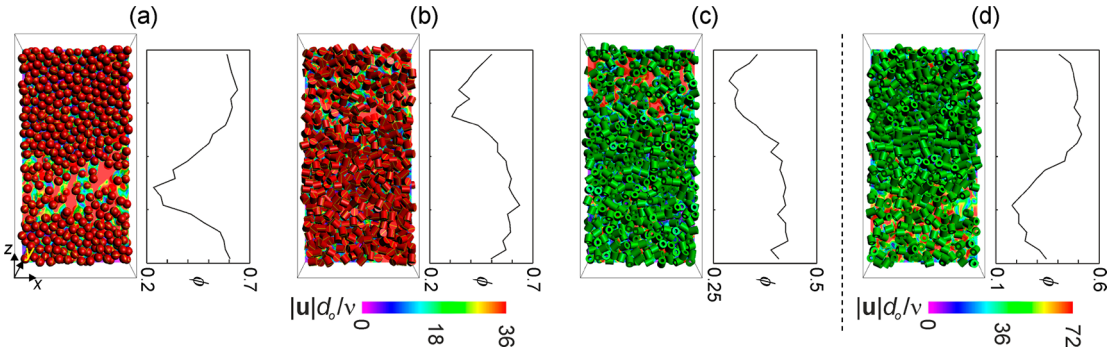

Figure 1. Single realizations of particles with their centers within a distance d from the xz-midplane and liquid velocity magnitude in the xz-midplane, and the associated profiles of the solids volume fraction averaged over x and y as a function of z. (a) Spheres with diameter d. (b) Solid cylinders with $l/d_c = 1$ and $d_e = d$. (c): Hollow cylinders with $l/d_o = 1$, $d_i/d_o = 0.5$, and $d_o = d_c$. In panels a–c, Ar = 5.63×10^3. (d) As in panel c, however, now Ar = 1.13×10^4. The overall solids volume fraction of the spheres and solid cylinder system is $\langle\phi\rangle = 0.50$; for the hollow cylinder system, it is 0.375.

is more complicated than for spheres. As the immersed boundary method, the algorithm for determining distance and relative velocity between particle surfaces makes use of marker points on particle surfaces[22] so that particle shape is explicitly accounted for when particles collide. In order to determine the direction of the interaction forces, each marker point is equipped with the outward normal vector of the particle surface at that location. In the present study only radial close-range interaction forces have been considered. At least for spheres, radial lubrication forces are significantly higher than tangential lubrication forces.[29] Having only radial—and therefore no tangential—dry collision forces implies that we assume the particle surfaces to be smooth and thus the friction coefficient to be zero. In the Supporting Information, expressions for close-range interaction forces and values of associated parameters are given.

(5) After updating particles' linear and angular velocity, their location and orientation need to be updated. Particles are being translated by a simple Euler forward rule. For keeping track of the particle orientation, each one of them has a quaternion[21] that is updated every time step according to the solution given in ref 30. The quaternions are specifically helpful for exchanging information (location, velocity, force, torque) between the (overall) inertial reference frame and the reference frames attached to the individual particles.[31]

4. SET-UP OF SIMULATIONS

As a reference case for which experimental data is available,[4] fluidization of spherical particles all having the same diameter d is considered. The spatial resolution is such that $d/\Delta = 16$; the temporal resolution is such that $\Delta t\nu/d^2 = 7.81 \times 10^{-5}$. The domain size is $12d \times 12d \times 24d$ in x, y, and z directions, respectively. With $n = 3300$ spheres this results in an overall solids volume fraction $\langle\phi\rangle = 0.50$. The density ratio is $\gamma = 4$. The Archimedes number is Ar = 5.63×10^3. To put this in perspective, this mimics fluidization of $d \approx 700$ μm spheres in water in the earth's gravitational field.[4]

The solid cylindrical particles that have been studied have the same density as the spheres, the same volume as the spheres (to a good approximation), and have an aspect ratio $l/d_c = 1$. This then implies that $l/\Delta = d_c/\Delta = 14$. The *equivalent* diameter of the solid cylinders is defined as $d_e = \sqrt[3]{3d_c^2 l/2}$ and for these cylinders is equal to the diameter $d$of the spheres. With the same kinematic viscosity of the fluid and the same gravitational acceleration these solid cylinders are characterized by the same Archimedes number as the spheres.

Three variants of hollow cylinders have been simulated. Hollow cylinders have three dimensions: outer diameter d_o, inner diameter d_i, and length l. All three cylinder variants have $d_o/d_i = 2$. The first variant has $d_o = d_c$ and $l/d_o = 1$ so that its volume is 3/4 that of the solid cylinder. With the same number $n = 3300$ of particles, this means $\langle\phi\rangle = 0.375$. By giving this hollow cylinder a density ratio $\gamma = 5$, it has the same Ar as the solid cylinders (as well as the spheres). The other two hollow cylinders have the same volume and density as the first one (and therefore again the same Archimedes number) but differ in their length-over-outer-diameter aspect ratio. One has $l/d_o = 0.56$; the other one has $l/d_o = 1.58$. It is important to note at this stage that we might have somewhat compromised our spatial resolution given that for the hollow cylinder with $l/d_o = 1.58$, the inner diameter spans only six lattice spacings ($d_i/\Delta = 6$).

Care has been given to initialize the particle configurations in a random fashion and so to speed up reaching a dynamically steady fluidization state. At the high solids volume fractions studied here, it would take significant (simulation) time for a system to "forget" its initial orderly state if it were initialized that way. To facilitate a random initial configuration, first we build random assemblies of spheres by placing them at random locations in a nonoverlapping way. This can only be done up to $\langle\phi\rangle \approx 0.3$[32] so that we subsequently need to compress the domain to reach the desired solids volume fraction. For (hollow) cylinder simulations we give the spheres a diameter of $\sqrt{d_o^2 + l^2}$ so that the sphere would completely encapsulate a cylinder. When starting the compression those spheres are replaced by randomly oriented cylinders, and we continue compressing until the desired volume fraction is reached.

For the hollow cylinders a parameter variation study has been conducted. As described above, there are three variants of hollow cylinders with $l/d_o = 0.56$, 1.0, and 1.58, respectively. All have the same volume, and all have $\gamma = 5$ and $d_o/d_i = 2$. In addition to the base-case Archimedes number of Ar = 5.63×10^3, three other values of Ar have been considered: 2.82×10^3, 8.45×10^3, and 1.13×10^4.

5. RESULTS

5.1. Fluidization of Spheres, Solid Cylinders, and Hollow Cylinders. In order to relate to previous simulation work of ours[12] and to experimental results,[4] a reference case of liquid fluidization of solid spheres was designed that—in a

https://doi.org/10.1021/acs.iecr.2c04464
Ind. Eng. Chem. Res. 2023, 62, 19197−19204

physical sense—is almost identical to one of the simulation cases discussed in ref 12. The main *numerical* difference is the collision algorithm that previously was hard-sphere and now is soft-sphere because that same soft-"sphere" (soft-particle) algorithm has been used in subsequent simulations of nonspherical particle fluidization. Another numerical difference compared to previous work is the domain size which is now twice as large in the lateral directions and 1.2 times larger in the vertical direction.

It is reassuring to see the development of a voidage wave traveling in the positive z-direction in the current simulation (see Figure 1a). Such waves have been observed experimentally in liquid fluidization in narrow columns[4] and were reproduced well previously by the algorithm that included hard-spheres.[12] It is important to note that the realizations in Figure 1 (and also in Figure 3) do not show all particles but only particles with their center in a $2d$ thick slice. The other panels of Figure 1 show that also fluidized cylindrical particles develop waves. In Figure 1b one sees an instantaneous realization of the voidage wave for fluidized solid cylinders with $l/d_c = 1$ and the same Archimedes number as the spheres. The wave in the fluid bed of hollow cylinders has less contrast in terms of solids volume fraction as a function of vertical location $\phi(z)$ (see Figure 1c). An increase of the Archimedes number deepens that wave (Figure 1d).

A quantitative analysis of the waves as shown in Figure 1 is presented in Figure 2. In its left panel it is illustrated how wave

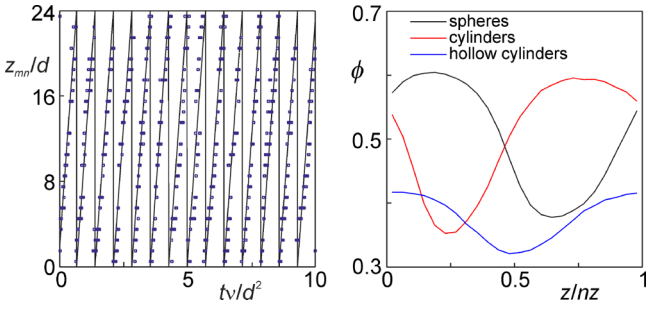

Figure 2. Left: symbols are z-locations of the minima in the $\phi(z)$ profiles at subsequent instantaneous realizations; the line is a linear fit taking into account periodic conditions in the z-direction; fluidization of spheres. Right: average voidage wave forms for the cases shown in Figure 1a,b,c. The dimensionless wave speeds for these cases are cd/ν = 33.3, cd_c/ν = 24.3, and cd_o/ν = 20.2, respectively. Given periodic conditions, the locations of the waveforms on the abscissa are arbitrary.

speeds have been determined. Solids volume fraction profiles $\phi(z)$ having a spatial resolution of one sphere diameter d (such as the ones shown in Figure 1) of a large number ($\sim 1.2 \times 10^3$) of realizations after dynamic steady state was reached were determined, and their minimum ϕ values were identified. The z-locations of the minima are plotted as a function of time, and a linear function was fitted to them. The slope of that line represents the wave speed c which for the spheres was found to be $cd/\nu = 33.3$. This is almost identical to the speeds found in the earlier hard-sphere simulations[12] (cd/ν = 33.7 for $\langle\phi\rangle$ = 0.505 and 33.2 for $\langle\phi\rangle$ = 0.488) and close to the experimental value of 29 ± 1.4.[4] Given the so determined wave speeds, average wave-profiles can be determined by taking a series of instantaneous profiles $\phi(z)$ at times t_i and shifting them in the negative z-direction over a distance ct_i (taking into account the periodic boundaries) and then averaging them. Examples of average wave profiles are shown in the right panel of Figure 2. The wave for the solid cylinders is at least as deep as the one for the spheres; its speed is significantly smaller (as noted in the caption of Figure 2). Given the holes in the hollow cylinders, their average volume fraction is less by 25% than that of the solid cylinders and the spheres. Their wave amplitude is less than 0.5 times the amplitude of both types of solid particles.

The fluidization characteristics of the other two hollow cylinders (with $l/d_o = 0.56$ and $l/d_o = 1.58 l/d_o = 1.58$) are shown in Figure 3. The most remarkable observation is that the longer hollow cylinders do not develop a wave if Ar = 5.63×10^3 and only a very shallow one if the Archimedes number is twice as high.

The results presented so far are for systems that are in a dynamic steady state. The development toward this state has been monitored by keeping time series of domain-average quantities. In Figure 4 we show two examples for solid cylindrical particles with $l/d_c = 1$: a time series of the domain-averaged slip velocity of the cylinders and their domain-averaged orientation angle. In addition, the figure shows time series of slip velocity and angle for one particle. The domain-average quantities get stable after a very short start-up period that lasts less than $0.5d_c^2/\nu$. Judging from the single-particle data, the velocity fluctuation levels are much higher than the average velocity. The periodicity that can be discerned from the single-particle velocity time series is due to that particle periodically encountering the voidage wave, with the negative spikes in velocity the moments the particle is falling through the void.

The orientation angle distributions of cylinders (solid and hollow) are in Figure 5 with the angle ψ the angle between the vertical direction and cylinder centerline. An isotropic orientation distribution has $\sin\psi$ as its distribution function.

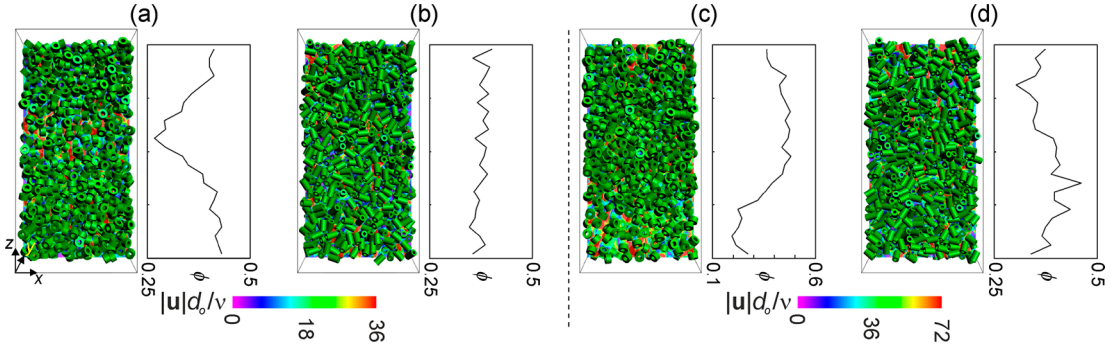

Figure 3. Single realizations of hollow cylinders with their centers within a distance d (the sphere diameter) from the xz-midplane and liquid velocity magnitude in the xz-midplane, and the associated profiles of the solids volume fraction averaged over x and y as a function of z. (a) $l/d_o = 0.56$ and Ar = 5.63×10^3. (b) $l/d_o = 1.58$ and Ar = 5.63×10^3. (c) $l/d_o = 0.56$ and Ar = 1.13×10^4. (d) $l/d_o = 1.58$ and Ar = 1.13×10^4.

https://doi.org/10.1021/acs.iecr.2c04464
Ind. Eng. Chem. Res. 2023, 62, 19197−19204

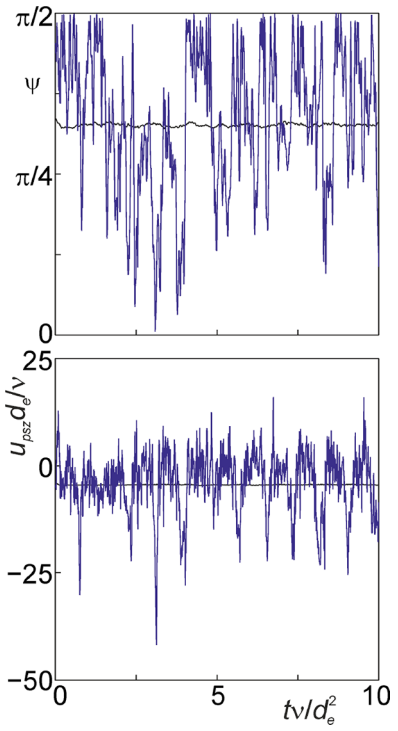

Figure 4. Time series of volume average data (black) and sample single-particle data (blue) for (top) the angle ψ of the centerline of cylinders with the vertical and (bottom) the vertical particle slip velocity u_{psz}; $t = 0$ is the start of the simulation with fluid and particles at rest. Solid cylinders with $l/d_c = 1$, $d_e = d$, and Ar = 5.63×10^3.

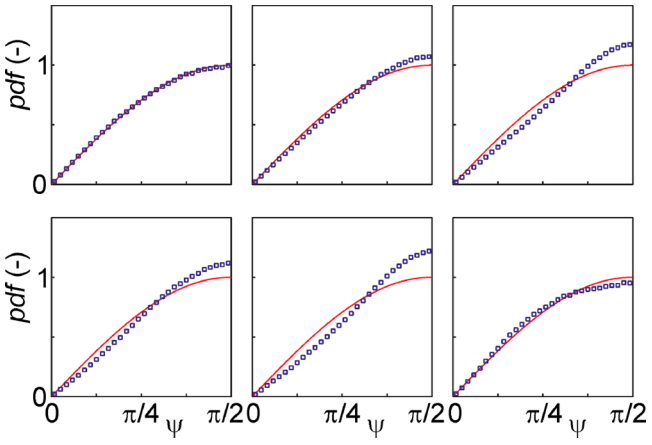

Figure 5. Probability density functions of the orientation angle ψ for solid cylinder (top) and hollow cylinder (bottom). From left to right $l/d_c = 0.56$, 1, and 1.58 (solid) and $l/d_o = 0.56$, 1, 1.58 (hollow). In all cases Ar = 5.63×10^3. The red curve is sin ψ, which is what an isotropic distribution of angles would look like.

One generally observes approximately isotropic distributions, very different from the preferentially vertical orientation of tall cylinders in settling suspensions.[22,33] In some cases shown in Figure 5, horizontal orientation is slightly overrepresented as compared to an isotropic distribution.

5.2. Flow in the Hollow Cylinders and Consequences for Mass Transfer. One reason for fluidizing hollow cylinders instead of solid cylinders (or solid particle in general) could be enhancement of transfer processes as a result of the flow within their inner diameter d_i. To investigate this internal flow we consider an instantaneous realization of the entire flow system. We identify the lattice nodes within the inner diameter of each cylinder, determine the fluid velocity at these nodes relative to the velocity of the cylinder, and focus on the relative velocity component in the axial direction of the cylinder (that we call the "1" direction). For each node inside the cylinder we determine its radial location relative to the centerline of the cylinder and its axial location relative to the middle of the cylinder. Averaging in the axial direction then gets us fluid velocity profiles $u_1(r)$ as in Figure 6. These are akin to Poiseuille profiles.

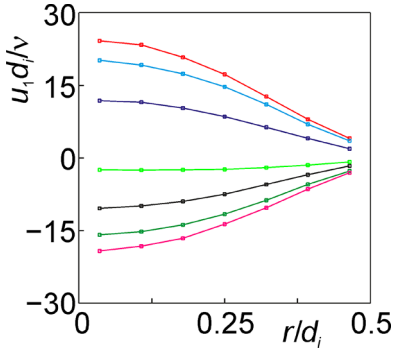

Figure 6. Radial profiles of fluid velocity inside six randomly selected hollow cylinders in an instantaneous realization of the flow system; $u_1(r)$ is the axial velocity component as a function of the radius r averaged over the length of the cylinder. Flow system with $l/d_o = 1$ and Ar = 5.63×10^3.

The average axial velocity in each cylinder $\langle u_1 \rangle$ follows from integration of $u_1(r)$ over the cross sectional area of its inner part. Before performing a more quantitative analysis regarding the flow through the cylinders we first make a few qualitative observations regarding $\langle u_1 \rangle$. Figure 7 correlates the cylinder

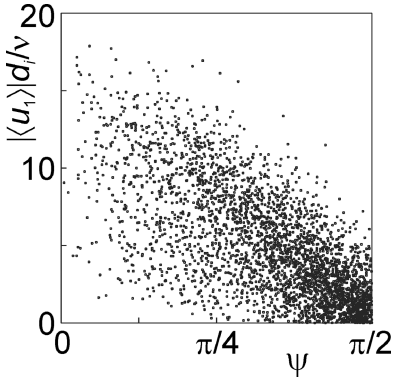

Figure 7. Each dot in this graph represents the orientation angle ψ of a cylinder versus the absolute value of the relative average axial flow velocity $|\langle u_1 \rangle|$ inside the cylinder for a single realization of the system with $l/d_o = 1$ and Ar = 5.63×10^3.

orientation angle ψ with $|\langle u_1 \rangle|$. We see large scatter which is the result of the random nature of particle and fluid motion and the resulting wide orientation angle distribution (see Figure 5). Overall, however, there is a trend of higher flow through cylinders that are oriented with smaller ψ, i.e., are closer to being vertical. This makes sense given that the mechanisms driving the flow are vertical (net gravity on particles down, body force $\mathbf{f} = \langle \phi \rangle (\gamma - 1)\rho g \mathbf{e}_z$ on fluid up). Figure 8 shows how flow through cylinders is sensitive to the uneven distribution of solids over the domain as a result of the voidage wave. In this figure we compare

https://doi.org/10.1021/acs.iecr.2c04464
Ind. Eng. Chem. Res. 2023, 62, 19197−19204

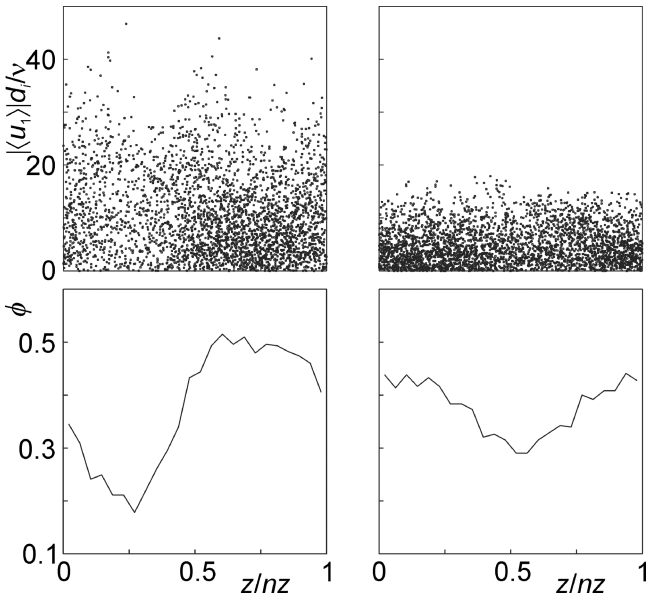

Figure 8. Top: the relative average axial flow velocity $|\langle u_1\rangle|$ inside the hollow cylinders correlated with their z-location. Bottom: the corresponding instantaneous solids volume fraction profile. Cylinders with $l/d_o = 1$. Left: Ar = 11.3×10^3; right Ar = 5.63×10^3.

two Ar values, with the higher value developing a much stronger wave than the lower one. This translates into a more inhomogeneous distribution of the strength of flow through cylinders with, interestingly, a larger probability for higher $|\langle u_1\rangle|$ there where the solids volume fraction gradient $|d\phi/dz|$ is largest, i.e., at the leading and trailing sides of the wave. At the leading edge, particles accelerate when they enter the void; at the trailing edge, they decelerate when—after falling through the void—fall onto the denser region, apparently leading to somewhat stronger flow through the cylinders. No such observation can be made for the weaker wave at the lower Archimedes number.

It is now hypothesized, as inspired by the velocity profiles in Figure 6, that the flow through the inner diameter of the cylinders can be described as a Poiseuille flow. To test this, we determined the driving force of the flow through each of the cylinders for single realizations of the simulations. This driving force has two contributions: in the first place, the component of the body force $\mathbf{f}$ in the axial direction (the 1-direction) of each cylinder ($f_1 = |\mathbf{f}| \cos \psi$); in the second place, the component of the pressure gradient $-\nabla p = -\mathbf{\Gamma}$ in that same direction ($-\Gamma_1$). The sum of these contributions would lead to an average velocity in the 1-direction of $\langle u_{P1}\rangle = \frac{(f_1 - \Gamma_1)d_i^2}{32\rho\nu}$ (with the subscript P in u_{P1} indicating that this is the Poiseuille velocity estimate).

In Figure 9, $\langle u_1\rangle$ and $\langle u_{P1}\rangle$ are compared for the three hollow cylinder variants for one instantaneous realization each. There is a clear correlation between $\langle u_1\rangle$ and $\langle u_{P1}\rangle$ with their level of quantitative agreement dependent on l/d_o. The more relevant aspect ratios are l/d_i, the length of the channel in the cylinder divided by its diameter. Given that in all cases $d_i/d_o = 0.5$, l/d_i is 3.16, 2.0, and 1.12 from left to right in Figure 9. One then can appreciate that the relatively good agreement between $\langle u_1\rangle$ and $\langle u_{P1}\rangle$ for $l/d_i = 3.16$ is a result of the weaker influence of entrance and exit effects for these longer channels. Along the same line of reasoning, the fact that very often $|\langle u_{P1}\rangle| > |\langle u_1\rangle|$ for $l/d_i = 1.12$ is

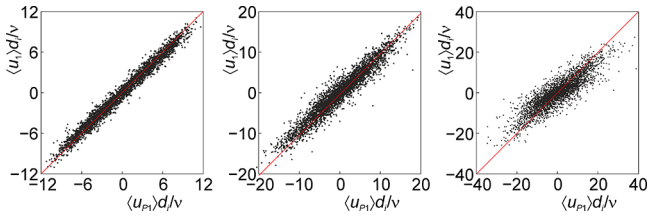

Figure 9. Actual average velocity $\langle u_1\rangle$ in hollow cylinders versus an estimate based on Poiseuille flow $\langle u_{P1}\rangle$. Each panel represents a single realization, and each dot represents one cylinder. From left to right l/d_o = 1.58, 1, 0.56. For all three cases Ar = 5.63×10^3.

due to extra pressure drop (better, extra driving force requirements) at the entrance and exit of the channel.

Based on the above we for now assume that to a good approximation the flow inside the hollow cylinders is a Poiseuille flow. This then opens an avenue for estimating mass transfer at the inner hollow cylinder surface. The main focus of this paper is on liquid fluidized systems, which means we are interested in mass transfer at high Schmidt numbers, i.e. at low mass (Fick) diffusion coefficients, which sets this work somewhat apart from much of the heat and mass transfer work that often involves gas−solid systems and Prandtl or Schmidt numbers of order one.[16,17,34] In the following it will be assumed that the Schmidt number $\mathrm{Sc} = \nu/\kappa = 1 \times 10^3$ with κ the diffusion coefficient. If it is then inferred that fluid residence time in the cylinder $l/|\langle u_1\rangle|$ is small compared to the time to achieve radial diffusion d_i^2/κ, we can use solutions to the Graetz problem[35] for estimating mass transfer coefficients (symbol k). The consequence of the solution when having a constant (inner cylinder) wall concentration can be expressed as $\langle \mathrm{Sh}\rangle = 1.62\left(\frac{|\langle u_1\rangle| d_i^2}{\kappa l}\right)^{1/3}$ with the Sherwood number defined as $\mathrm{Sh} = kd_i/\kappa$ and the angled brackets denoting an average over the length l of the channel. As a rule of thumb it is demanded that $\frac{\kappa l}{|\langle u_1\rangle| d_i^2} < 0.05$ for the above Sherwood correlation to be reasonably accurate. If a Reynolds number is defined as $\mathrm{Re} = |\langle u_1\rangle| d_i/\nu$, the Sherwood correlation can also be written as $\langle \mathrm{Sh}\rangle = 1.62\mathrm{Re}^{1/3}\mathrm{Sc}^{1/3}(l/d_i)^{-1/3}$.

We now take instantaneous realizations of our simulations and determine $|\langle u_1\rangle|$ for every hollow cylinder. We check the condition $\frac{\kappa l}{|\langle u_1\rangle| d_i^2} < 0.05$ and, if it holds, calculate $\langle \mathrm{Sh}\rangle$ for that cylinder and include it in the determination of the volume-average Sherwood number $\langle\langle \mathrm{Sh}\rangle\rangle$. The results are shown in Figure 10. Each of the symbols in that figure is the average of four

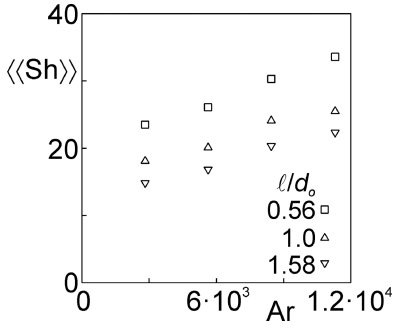

Figure 10. Average Sherwood number associated with mass transfer inside hollow cylinders as a function of Archimedes number for three values of l/d_o as indicated and for a Schmidt number of Sc = 1×10^3.

https://doi.org/10.1021/acs.iecr.2c04464
Ind. Eng. Chem. Res. 2023, 62, 19197−19204

instantaneous realizations. The differences in $\langle\langle \mathrm{Sh} \rangle\rangle$ between realizations are very small (less than 1%) so that error bars in the figure would be smaller than the size of the symbols. At least 99% of the cylinders satisfy the criterion $\frac{\kappa l}{|\langle u_i \rangle| d_i^2} < 0.05$ in any of the realizations involved in Figure 10. Most (of the few) cylinders that do not satisfy the criterion have $l/d_o = 1.58$. These are the ones with the longest and narrowest channels.

Average Sherwood numbers $\langle\langle \mathrm{Sh} \rangle\rangle$ are in the range 15−35, and they increase with increasing Ar. The three hollow cylinders we compare all have the same volume. Decreasing the l/d_o has a profound positive effect on $\langle\langle \mathrm{Sh} \rangle\rangle$ inside the cylinders. If we think, however, in terms of ka, i.e., mass transfer coefficient times (specific) surface area, we find that $ka \propto \langle\langle \mathrm{Sh} \rangle\rangle l\kappa$ and the larger l then compensates the lower $\langle\langle \mathrm{Sh} \rangle\rangle$ for the longer cylinders.

It is beyond this paper to perform mass transfer calculations at the outer surfaces of the cylinders and compare their Sherwood numbers with the internal ones. It would require solving a scalar transport equation in conjunction with our flow simulation with−given the high Schmidt number−a spatial resolution much higher than the resolution of the flow dynamics simulation. We previously have attempted this for spherical particles at lower solids volume fractions ($\langle\phi\rangle$ up to 0.30) by using coupled overlapping domains where a very fine spherical mesh is used to solve the (scalar) convection diffusion equation around each particle.[19] It is possible to follow a similar strategy for particles with shapes different from spheres. However, it needs further investigation to find out how the strategy would perform at the higher solids volume fractions of $\langle\phi\rangle = 0.5$ that have a much closer spacing between particles.

In order to have an order-of-magnitude estimate of mass transfer at the outer cylinder surfaces we revert to the correlation proposed by Gunn:[36]

$$\langle\langle \mathrm{Sh} \rangle\rangle = (7 - 10\varepsilon + 5\varepsilon^2)(1 + 0.7\mathrm{Re}_p^{0.2}\mathrm{Sc}^{1/3}) + (1.33 - 2.4\varepsilon + 1.2\varepsilon^2)\mathrm{Re}_p^{0.7}\mathrm{Sc}^{1/3}$$

with $\varepsilon = 1 - \langle\phi\rangle$ the voidage and Re_p a particle-based Reynolds number. The correlation is applied to the system considered in Figure 4 that has solid cylinders with $l/d_c = 1$ and $\mathrm{Ar} = 5.63 \times 10^3$. For Re_p in the Gunn-correlation we take the absolute value of the steady part of the average dimensionless velocity time series: $\mathrm{Re}_p \approx 4$ (i.e., we take the equivalent diameter d_e as the length scale in Re_p). With $\varepsilon = 0.5$ and $\mathrm{Sc} = 1 \times 10^3$ this gives $\langle\langle \mathrm{Sh} \rangle\rangle \approx 40$. The hollow cylinder with the same mass and aspect ratio at the same Archimedes number has an internal Sherwood number of $\langle\langle \mathrm{Sh} \rangle\rangle \approx 20$ so that the internal surface would contribute significantly to the overall mass transfer performance of the particle.

6. CONCLUSIONS

In this paper we explore, through particle-resolved simulation, the liquid fluidization behavior of short cylindrical particles (solid and hollow) building upon experiments[4] and simulations of liquid fluidization of spheres under similar conditions. In the simulations the particles are free to translate and rotate. They collide by means of a soft-particle algorithm. To compensate for lack of resolution of the flow in the narrow spaces between particles, radial lubrication forces are included in the equations of motion of each particle. Conditions are such that instabilities develop with the waveforms for solid cylinders comparable to those for spheres but with different wave speeds. The wave speeds for the spheres system compare favorably with experimental data.[4] At the same Archimedes numbers, hollow cylinders generate waves that are less pronounced than their solid cylinder counterparts or do not generate waves at all. The orientation distribution of the short cylinders is close to isotropic.

It is demonstrated that the flow inside the inner diameter of hollow cylinders is akin to Poiseuille flow given the shape of its axial fluid velocity profile with radial location, as well as the way the average axial velocity scales with the driving force. The average velocity in the cylinders is sensitive to their orientation angle with, on average, higher speeds for more vertically oriented cylinders and is sensitive to inhomogeneities induced by the voidage waves.

Under the assumption of Poiseuille flow and with liquids with high Schmidt numbers ($\mathrm{Sc} = 1 \times 10^3$ in this paper), we make use of solutions to Graetz problems to estimate the mass transfer potential of the inner cylinder surfaces and study the dependency of Sherwood numbers on Archimedes number and on aspect ratios of the hollow cylinder geometries. We observe inner cylinder Sherwood numbers that are of the same order of magnitude as those to be estimated for the external particle surfaces so that mass transfer enhancement is to be expected with hollow cylinders as compared to solid ones.

It is one of the intentions of this paper to try and raise the interest of experimentalists for generating and sharing experimental data on systems similar to the ones studied in this paper that could be used for comparison with numerical results: wave speeds and wave forms and their sensitivity to particle shape. We also would welcome experimental data that could challenge some of the trends regarding mass transfer as identified in this paper—additional mass transfer for hollow cylinders and the effects of hollow cylinder aspect ratios on mass transfer. Future work on the simulation side will initially deal with computational efficiency to be able to enhance the resolution and thereby the accuracy of the simulations.

■ ASSOCIATED CONTENT

Supporting Information

The Supporting Information is available free of charge at https://pubs.acs.org/doi/10.1021/acs.iecr.2c04464.

Information on short-range interaction force expressions and parameter settings (PDF)

■ AUTHOR INFORMATION

Corresponding Author

Jacobus Johannes Derksen − *School of Engineering, University of Aberdeen King's College, Aberdeen AB24 3UE, United Kingdom;* orcid.org/0000-0002-9813-356X; Email: jderksen@abdn.ac.uk

Complete contact information is available at: https://pubs.acs.org/10.1021/acs.iecr.2c04464

Notes

The author declares no competing financial interest.

■ REFERENCES

(1) Kunii, D.; Levenspiel, O.*Fluidization Engineering*, 2nd ed.; Butterworth-Heinemann: Oxford, 1991.

(2) Ranade, V.; Chaudhari, R.; Gunjal, P. R.*Trickle Bed Reactors*; Elsevier: Amsterdam, 2011.

(3) Di Felice, R.Liquid fluidization. Chapter 3 in *Essentials of Fluidization Technology*; Grace, J, Bi, X., Eds.; Wiley, 2020.

(4) Duru, P.; Nicolas, M.; Hinch, J.; Guazzelli, E. Constitutive laws in liquid-fluidized beds. *J. Fluid Mech.* **2002**, *452*, 371.
(5) Duru, P.; Guazzelli, E. Experimental investigations on the secondary instability of liquid fluidized beds and the formation of bubbles. *J. Fluid Mech.* **2002**, *470*, 359.
(6) Andersson, A.; Holmberg, J.; Haggblad, R. Process improvements in methanol oxidation to formaldehyde: application and catalyst development. *Topics Catalysis* **2016**, *59*, 1589.
(7) Partopour, B.; Dixon, A. G. Effect of particle shape on methanol partial oxidation in a fixed bed using CFD reactor modeling. *AIChE J.* **2020**, *66*, No. e16904.
(8) Lu, L.; Yu, J.; Gao, X.; Xu, Y.; Shahnam, M.; Rogers, W. A. Experimental and numerical investigation of sands and Geldart A biomass co-fluidization. *AIChE J.* **2020**, *66*, No. e16969.
(9) Chen, X.; Zhong, W.; Heindel, T. J. Using stereo XPTV to determine cylindrical particle distribution and velocity in a binary fluidized bed. *AIChE J.* **2019**, *65*, 520.
(10) Fotovat, F.; Ansart, R.; Hemati, M.; Simonin, O.; Chaouki, J. Sand-assisted fluidization of large cylindrical and spherical biomass particles: Experiments and simulation. *Chem. Eng. Sc.* **2015**, *126*, 543.
(11) Werther, J.; Reppenhagen, J. Catalyst attrition in fluidized-bed systems. *AIChE J.* **1999**, *45*, 2001.
(12) Derksen, J. J.; Sundaresan, S. Direct numerical simulations of dense suspensions: wave instabilities in liquid-fluidized beds. *J. Fluid Mech.* **2007**, *587*, 303.
(13) Uhlmann, M. Interface-resolved direct numerical simulation of vertical particulate channel flow in the turbulent regime. *Phys. Fluids* **2008**, *20*, No. 053305.
(14) Wang, D.; Jin, T.; Luo, K.; Fan, J. An improved direct-forcing immersed boundary method for simulations of flow and heat transfer in particle-laden flows. *I. J. Multiphase Flow* **2022**, *153*, 104139.
(15) Euzenat, F.; Hammouti, A.; Climent, E.; Fede, P.; Wachs, A. Fluid-particle heat transfer in static assemblies: Effect of particle shape. *I. J. Heat & Fluid Flow* **2021**, *92*, 108873.
(16) Chang, Q.; Yang, L.; Ge, W. Fluid-particle heat transfer in static assemblies: Effect of particle shape. *I. J. Heat & Mass Transfer* **2021**, *166*, 120730.
(17) Lu, J.; Peters, E. A. J. F.; Kuipers, J. A. M. Direct numerical simulation of mass transfer in bidisperse arrays of spheres. *AIChE J.* **2020**, *66*, e16786.
(18) Lu, J.; Zhu, X.; Peters, E. A. J. F.; Verzicco, R.; Lohse, D.; Kuipers, J. A. M. Moving from momentum transfer to heat transfer − A comparative study of an advanced Graetz-Nusselt problem using immersed boundary method. *Chem. Eng. Sc.* **2019**, *198*, 317.
(19) Derksen, J. J. Simulations of solid-liquid mass transfer in fixed and fluidized beds. *Chem. Eng. J.* **2014**, *255*, 233.
(20) Uhlmann, M. An immersed boundary method with direct forcing for the simulation of particulate flows. *J. Comput. Phys.* **2005**, *209*, 448.
(21) Kuipers, J. B.*Quaternions and Rotation Sequences*; Princeton University Press: Princeton, 1999.
(22) Derksen, J. J. Liquid fluidization with cylindrical particles: Highly resolved simulations. *AIChE J.* **2019**, *65*, e16594.
(23) Somers, J. A. Direct simulation of fluid flow with cellular automata and the lattice-Boltzmann equation. *Appl. Sc. Res.* **1993**, *51*, 127.
(24) Eggels, J. G. M.; Somers, J. A. Numerical simulation of free convective flow using the lattice-Boltzmann scheme. *Int. J. Heat & Fluid Flow* **1995**, *16*, 357.
(25) Succi, S.*The lattice Boltzmann equation for fluid dynamics and beyond*; Oxford University Press Oxford, 2001.
(26) Ten Cate, A.; Nieuwstad, C. H.; Derksen, J. J.; Van den Akker, H. E. A. PIV experiments and lattice-Boltzmann simulations on a single sphere settling under gravity. *Phys. Fluids* **2002**, *14*, 4012.
(27) Feng, Z. G.; Michaelides, E. Robust treatment of no-slip boundary condition and velocity updating for the lattice-Boltzmann simulation of particulate flows. *Comp. & Fluids* **2009**, *38*, 370.
(28) Nguyen, N.-Q.; Ladd, A. J. C. Lubrication corrections for lattice-Boltzmann simulations of particle suspensions. *Phys. Rev. E* **2002**, *66*, No. 046708.
(29) Kim, S.; Karrila, S. J.*Microhydrodynamics: principles and selected applications*; Butterworth-Heinemann: Oxford, 1991.
(30) Phillips, W. F.; et al. Review of attitude representation used for aircraft kinematics. *J. Aircraft* **2001**, *38*, 718.
(31) Shardt, O.; Derksen, J. J. Direct simulations of dense suspensions of non-spherical particles. *Int. J. Multiphase Flow* **2012**, *47*, 25.
(32) Torquato, S.; Truskett, T. M.; Debenedetti, P. G. Is random close packing of spheres well defined? *Phys. Rev. Lett.* **2000**, *84*, 2064.
(33) Herzhaft, B.; Guazzelli, E. Experimental study of the sedimentation of dilute and semi-dilute suspensions of fibres. *J. Fluid Mech.* **1999**, *384*, 133.
(34) Cao, Z.; Tafti, D. K. Particle scale investigation of influencing factors on heat transfer in nonspherical particle−fluid system. *J. Heat Transfer* **2022**, *144*, No. 082701.
(35) Deen, W. M.*Analysis of transport phenomena*; Oxford University Press: Oxford, 1998.
(36) Gunn, D. J. Transfer of heat or mass to particles in fixed and fluidised beds. *Int. J. Heat Mass Transfer* **1978**, *21*, 467.

https://doi.org/10.1021/acs.iecr.2c04464
Ind. Eng. Chem. Res. 2023, 62, 19197−19204